Aerosol Science and Technology

ISSN: 0278-6826 (Print) 1521-7388 (Online) Journal homepage: www.tandfonline.com/journals/uast20

Experimental characterization of the electrostatic charge of aircraft engine emissions using conventional and sustainable fuels

Fergus O. N. Lidstone-Lane, Eliot Durand, Doğuşhan Kılıç, George McPherson, Andrew P. Crayford, Mark Johnson, Amanda Lea-Langton & Paul I. Williams

To cite this article: Fergus O. N. Lidstone-Lane, Eliot Durand, Doğuşhan Kılıç, George McPherson, Andrew P. Crayford, Mark Johnson, Amanda Lea-Langton & Paul I. Williams (11 Dec 2025): Experimental characterization of the electrostatic charge of aircraft engine emissions using conventional and sustainable fuels, Aerosol Science and Technology, DOI: 10.1080/02786826.2025.2596908

To link to this article: https://doi.org/10.1080/02786826.2025.2596908

AEROSOL SCIENCE AND TECHNOLOGY
https://doi.org/10.1080/02786826.2025.2596908

Experimental characterization of the electrostatic charge of aircraft engine emissions using conventional and sustainable fuels

Fergus O. N. Lidstone-Lane[a], Eliot Durand[b], Doğuşhan Kılıç[a,c], George McPherson[b], Andrew P. Crayford[b], Mark Johnson[d], Amanda Lea-Langton[e], and Paul I. Williams[a,c]

[a]Department of Earth and Environmental Sciences, University of Manchester, Manchester, UK; [b]Cardiff School of Engineering, Cardiff University, Cardiff, Wales, UK; [c]National Centre for Atmospheric Science, Manchester, UK; [d]Rolls-Royce plc, Derby, UK; [e]Department of Mechanical, Aerospace and Civil Engineering, University of Manchester, Manchester, UK

ABSTRACT

Aircraft gas turbines engines produce ions through chemiionization thought to result in electrostatically charged engine exhaust emissions. Most combustion systems generate a symmetrical bipolar charge distribution. However, due to high temperatures and pressures in aviation combustors, associated fast residence times, and high post-flame temperatures, aircraft emissions have been predicted to exhibit an asymmetrical bipolar charge distribution. It is thought this asymmetry tends toward a positive polarity, resulting from an increase in post-flame thermal ionization. This study employed an Electrostatic Precipitator and a Scanning Mobility Particle Sizer to determine the charged fraction, and an electrometer to determine the mean charge per particle of aircraft emissions. Three aircraft engines were assessed across a number of powers for conventional and sustainable aviation fuels. In agreement with previous theoretical studies, the measured emissions were found to be charged, resulting in up to 58.1% of the emissions being charged, which correlated with engine power. The charge distribution of aircraft emission was observed to be asymmetrical, tending toward positive polarities at higher powers (combustor temperatures). Along with power, it was noted that particle size was a key parameter driving the charge. As such, a fuel dependence was found, whereby emissions produced by JetA-1 typically carried 11–17% more charge compared to SAF for similar conditions, which was attributed to the reduced particle sizes in SAF emissions. Differences in charge was observed between the different engines; however, variations in the respective emissions sampling systems may have contribute to the findings, resulting in uncertainties associated with dynamical unsteady charging.

GRAPHICAL ABSTRACT

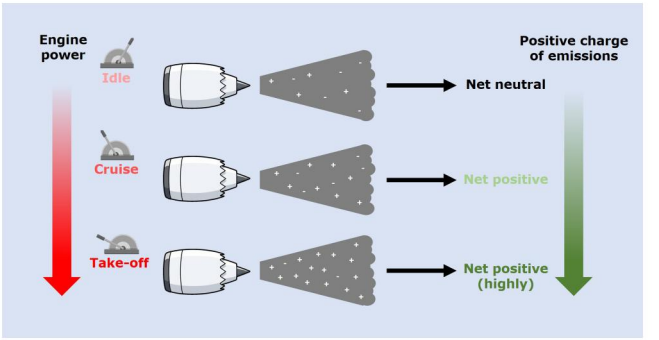

ARTICLE HISTORY
Received 25 February 2025
Accepted 4 November 2025

EDITOR
Olfert Jason

CONTACT Fergus O. N. Lidstone-Lane Fergus.lidstone-lane@postgrad.manchester.ac.uk Department of Earth and Environmental Sciences, University of Manchester, Simon Building, Brunswick Street, Manchester M13 9PS, UK.

Supplemental data for this article can be accessed online at https://doi.org/10.1080/02786826.2025.2596908.

1. Introduction

Aircraft gas turbine combustion engines produce harmful gaseous, volatile, and nonvolatile Particulate Matter (nvPM) emissions, resulting from incomplete combustion and evaporation of hydrocarbon-based fuels. It is well documented that this process generates a substantial amount of positively and negatively electrostatically charged molecular cluster also referred to as ions through chemiionization of hydrocarbons in fuels (Fialkov 1997; Burtscher 1992), predominantly *via* $CH + O \rightarrow CHO^+ + e^-$ reactions (Calcote 1962; Green and Sugden 1963). Further to the production of these primary ions, a complex array of heavier ions can be generated depending on the fuel composition, combustion conditions, and emissions residence times through the engine (Burtscher 1992; Haverkamp et al. 2004; Kittelson et al. 1986; Savel'ev et al. 2004). From the combustion generated ions, the emitted particles can become charged *via* attachment of the ions onto the particles (Burtscher 1992; Sorokin et al. 2003). The particles can also become charged *via* several other mechanisms including, charged particle recombination, charged-enhanced coagulation, and thermal ionization from hot surfaces in the post-flame region (Sorokin et al. 2003; Hayhurst and Kittelson 1978). In most combustion systems, the emissions have been measured to be highly charged, carrying a symmetrical bipolar charge distribution, as a result of the various aforementioned charging mechanisms (Fialkov 1997; Maricq 2006; Sgro et al. 2010). For example, it has been reported that over 40% of the particles are charged in the post-flame region of a premixed ethylene flame (Maricq 2004) and over 70% in diesel engine exhausts (Jung and Kittelson 2005; Kittelson et al. 1986).

In aircraft engine combustors, similar charging processes are anticipated, although due to the elevated combustion conditions, exhibiting temperatures in the range of 2,000 K (Chevron 2007) and pressure ratios of 40:1 (Correa 1998), a wider range of ions are expected (Keindler et al. 2000; Keindler and Arnold 2002). Furthermore, these combustion conditions have also been predicted to cause an asymmetrical charge distribution (Sorokin and Arnold 2004; Starik 2008; Vatazhin et al. 2004) resulting from the high combustor and post-flame temperatures (Sorokin et al. 2003). This is anticipated to lead to positively charged emissions due to an increase in thermal ionization (Sorokin and Arnold 2004), coupled with short residence times, which suppresses ion recombination and charge neutralization (Lukachko et al. 1998; Savel'ev and Starik 2001; Starik 2008). However, once the emissions exit the engine, the charge distribution is thought to tend to an symmetrical charge distribution downstream of the engine in the exhaust plume (Vatazhin et al. 2004).

To the authors' knowledge, to-date the charge state of total aircraft gas turbine emissions has not been investigated experimentally. Previous research characterizing the charge of aviation emissions has predominantly utilized chemical modeling-based approaches (Sorokin et al. 2003; Starik 2008; Vatazhin et al. 2004), with a few experimental studies quantifying the ion concentrations emitted downstream of the engine exit (Arnold et al. 1998; Sorokin and Arnold 2004). As such, the charge distribution of aircraft emissions has yet to be empirically assessed, particularly in the case of Sustainable Aviation Fuels (SAFs).

If aircraft emissions are exhibited to be highly charged, there are numerous potential implications, concerning environmental and human health effects, in addition to unquantified uncertainties associated with regulatory emission measurements. In terms of the environmental impacts, the charge of ions, nvPM, and volatile nucleation is thought to be a major contributing parameter to contrail formation (Ponsonby et al. 2024; Yu and Turco 1997, 1998). One process involves electrically charged particles acting as nucleation sites increasing the uptake of polar volatiles, such as water (Savel'ev and Starik 2001; Yu and Turco 1999). Human health effects also need to be considered, as it has been found that charged particles are more likely to penetrate through mucus layers and into the alveoli deep in the lungs (Zhu et al. 2024). Charged particles may also cause additional uncertainties associated with particle transport and measurement in regulatory sampling and measurement systems. Lidstone-Lane et al. (2025) found that electrostatic particle losses could occur through low conductivity sampling tubing (typical of aircraft emissions sampling and measurement systems) if the particles are sufficiently charged, leading to under-quantification of reported regulatory aviation emissions.

For this study, the charge of freshly emitted aircraft emissions was experimentally characterized for a Gnome turboshaft helicopter engine tested at Rolls-Royce Derby (UK), and both a Honeywell ALF502-R and a LF507-1H turbofan engine operated at a CFS Aeroparts test stand located at Hawarden Airport (UK). The Gnome engine was operated solely with JetA-1, while the ALF-502-R and LF507-1H were operated with two JetA-1 and two SAF blends (50% HEFA (Hydroprocessed Ester and Fatty acid)/JetA-1) from different sources. The charge was characterized using two parameters: charged fraction, which determines the number of charged particles, and the mean charge per particle: which gives a measure of the mean or net

charge of the emissions. The charged fraction was measured by employing an Electrostatic Precipitator (ESP), to remove all charged emissions from an aircraft emissions sample, then using a Scanning Mobility Particle Sizer (SMPS) and Condensation Particle Counter (CPC) to measure the particle number concentrations, similar to methods employed by Jung and Kittelson (2005) for automotive diesel engine emissions. For the mean charge per particle, a Faraday cup aerosol electrometer was used to measure the electrical current of the an aircraft emissions sample, and using the particle number concentration from a CPC, an estimated mean charge per particle was calculated, using a similar method proposed by Nishida et al. (2020). In addition, the uncertainties related to measuring the charge and the impact this may have on aircraft emissions sampling systems is presented. This study therefore informs better understanding of how aircraft emissions impact contrail formation, human health, and regulatory measurement uncertainty.

2. Methodology

The experimental data was acquired over two test campaigns at two different locations. Note that at the two different test campaigns, bespoke sampling systems were used, which incorporate some differences due to equipment avaibility and experimental constraints - details of the respective set-ups are presented in Figure 1. Over the course of the two campaigns, the charge of the emissions produced from three different engines running on five different fuels, as will be outlined in Section 2.2, were measured. As shown in Figure 1, for both campaigns, a similar suite of measurement instruments were used to measure the charged fractions and mean charge per particle of the emissions, which comprised of an ESP, SMPS, electrometer, and a CPC.

All tubes between instruments shown in Figure 1 were either made from stainless steel or conductive silicone, to reduce potential electrostatic losses occurring that may affect the final charge measurements (Lidstone-Lane et al. 2025). The overall tube lengths were kept to a minimum to reduce additional particle losses. Note the provided flowrates in Figure 1, for the engine probe sections are minimum values, typical at idle engine conditions only. As the engine power increased, the increasing dynamic pressure would have resulted in uncharacterized larger flowrates with associated reduced residence times in the initial tubing. The flowrate into the ESP was 3 L/min, providing 1 L/min for each of the measurement instruments (SMPS, electrometer, and CPC).

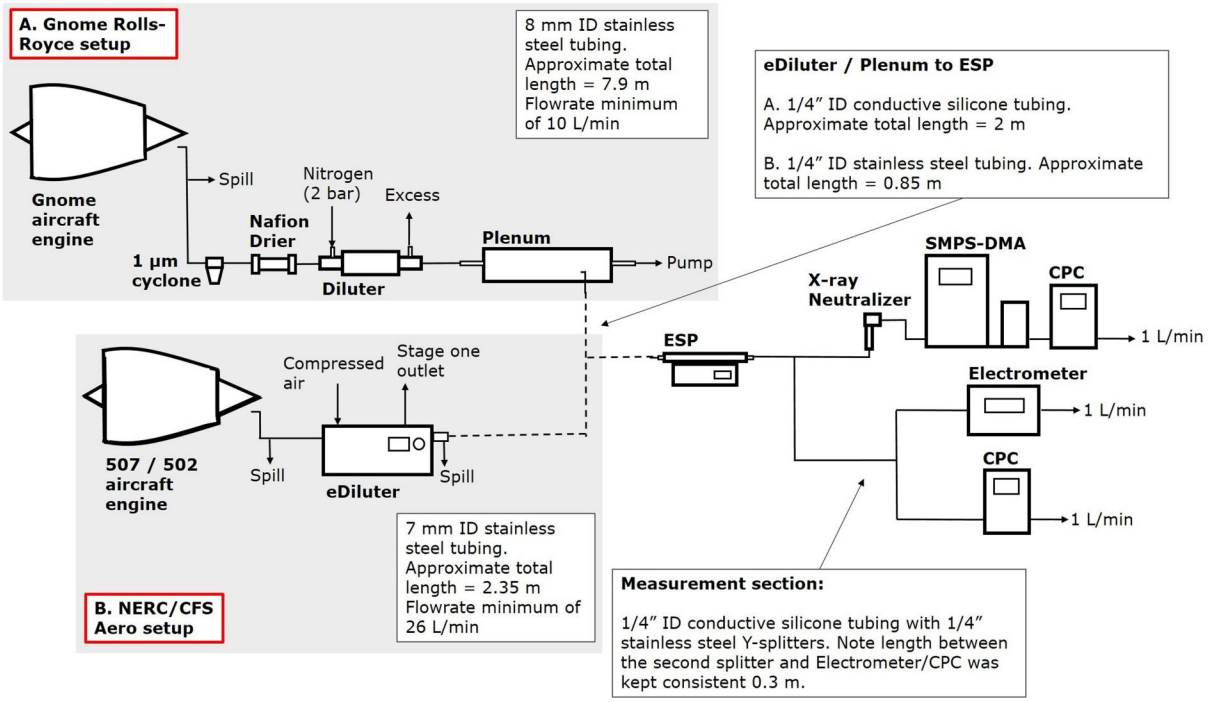

Figure 1. Schematic representation of the experimental set-ups used to determine the charge of (a) Gnome turboshaft helicopter engine and (b) Honeywell AFL502 (502) and LF507 (507) turbofan engines. The main differences between the sampling systems were the dilution systems used (DI-1000 for the Gnome and eDiluter for the 502/507), the length of the tubing, and the diameter of the tubing. Some additional sampling system instruments were used for the Gnome test (cyclone, drier, and plenum), but these instruments were assumed to have only minor effect on the measurements.

2.1. Charged fraction and mean charge per particle measurements

The measurement system used to determine both the charged fraction and mean charge per particle for all three engines, is shown (unshaded area) in Figure 1. The first part of the system was a Cambustion ESP, operated at 1700 V when on and 0 V when off. From the ESP, the sample flow was split *via* a 1/4" stainless steel two-way Y-splitter, with 1 L/min supplying the SMPS consisting of a TSI 3088 soft X-ray neutralizer, TSI 3082 SMPS, TSI 3085 nano Differential Mobility Analyzer (DMA) or a TSI 3081 long DMA, and a TSI 3750 CPC. The SMPS was operated to perform two 60 s scans, with both multiple charging and diffusional loss corrections applied. The nano DMA (particle size range of 6.5–80 nm) was initially used to measure the emissions of the 507 engine (and also the 502 for one of the fuels – SAF blend.2) as it was anticipated the measureable particle size range available would suitably cover the emitted particles. However, to ensure any larger particles emitted were measured, for the remaining 502 engine and all of the Gnome engine tests, the long DMA (particle size range of 7.5–414 nm) was used. For both DMA configurations, the bin width was set at the default of $1/64^{th}$ of a decade per each particle channel, with the sheath flow set to 10 L/min to meet the 10:1 sheath to inlet flow recommended by the manufacturer (TSI 2016). All instruments were assumed to be operating at the TSI Standard Temperature and Pressure (STP) in the instrument software −21.1 °C and 101.3 kPa (TSI 2016). Although the temperature and pressure assumptions may have resulted in some uncertainty in the measurements given slight discrepancies in day-to-day ambient conditions. The d_{50} of the TSI 3750 CPC was 7.5 nm, and thus values below this range were discounted. From the ESP, the remaining flow of 2 L/min was directed and split evenly to a TSI 3068B Faraday Cup electrometer and a TSI 3750 CPC *via* another 1/4" stainless steel two-way Y-splitter. The flow through the CPCs and the electrometer was maintained by an external vacuum pump coupled with a critical orifice (CPC) or internal flow controller (electrometer). It is noted that the flow control may have impacted the accuracy of the measurements particularly impacting the mean charge per particle parameter due to the accuracy of the electrometer flow controller. To limit this impact, the flowrates of the respective CPCs and electrometer were measured at the beginning of each test campaign, which were observed to be within 5% of the reported values – see the online supplementary information (SI).

Two measurements were conducted to empirically quantify the charge of the aircraft engine emissions: the charged fraction and the mean charge per particle. Two charged fraction parameter were determined: the charged fraction of the total particle population (F_q) and as a function of particle diameter ($F_q(N(d_p))$). Both of these charged fraction methodologies did not distinguish between the charge polarity, only whether the emissions were charged or not. By taking the total particle number concentrations from the CPC when the ESP was turned on (N_{un}) and off (N_{total}), the total charged fraction for the emissions was calculated by:

$$F_q = \frac{N_{total} - N_{un}}{N_{total}} \quad (1).$$

In a similar manner, the charged fraction as a function of particle diameter was determined by measuring the particle size distribution using the SMPS when the ESP was turned on ($N(d_p)_{un}$)) and turned off ($N(d_p)_{total}$), and calculated by:

$$F_q\left(N\left(d_p\right)\right) = \frac{N\left(d_p\right)_{total} - N\left(d_p\right)_{un}}{N\left(d_p\right)_{total}} \quad (2).$$

Using the measurement of the total particle number concentration (*N*total) from the CPC and the total electrometer current (*i*), the final mean charge per particle was calculated from:

$$\overline{q} = \frac{i}{N_{total}\ Q\ e} \quad (3),$$

where *e* is the elementary charge (1.602E-19 C) and *Q* is the flowrate passing through the electrometer.

To increase the accuracy of the measurements, a 30 s test point at a sampling rate of 1 Hz was taken only when the recorded data from both the CPC and electrometer outputs were observed to be stable. Where possible, two 60 s SMPS scans, and thus 120 s CPC and electrometer samples, for ESP turned on and off were recorded. However, for some of the test points for higher engine powers, particularly when running the 502 and 507 engines, only one SMPS scan for each ESP setting was obtained, due to practicality and financial considerations. When permitted, multiple repeat measurements of the engines were conducted – mostly at the test points for lower power engine conditions, where engine wear and fuel costs were less significant. For each test point, the measured values were averaged over the chosen 30 s sample time. The uncertainty, shown by error bars in the results presented below, was determined from the variability of the data by calculating one standard deviation of the recorded data across the chosen sample time. Where multiple measured samples were used

to determine a parameter, the uncertainties were propagated through each measured sample – see the SI for an outlined methodology.

The charged fraction as a function of particle size measurements were compared against a theoretical bipolar aerosol charged fraction prediction proposed by Wiedensohler (1988). This prediction provides a valid approximation of a bipolar charge distribution on an aerosol population in air at ambient conditions post an aerosol neutralizer. Therefore, comparing the measured charged fraction as a function of particle size against this theoretical prediction provides an indication of whether the investigated aircraft engine emissions exhibits a bipolar charge distribution similar to one produced by an aerosol neutralizer.

2.2. Honeywell ALF502 (502) and LF507 (507) turbofan engine experiment

The Honeywell ALF502-R (502) and Honeywell LF507-1H (507) turbofan aircraft engines were both tested at the CFS Aeroparts facility located at Hawarden Airport near Chester (UK) over a two-week test period in September 2023. The 502 and 507 engines incorporate similar technology, both using reverse flow annular combustors to produce ~30 kN of thrust. However, it is noted the 502 engine had only one low pressure compressor (CFS Aeroproducts 2022), compared to the two incorporated in the 507 engine (Allied Signals Aerospace 1996), which results in a marginally lower thrust. For these studies, a bespoke equal area multipoint (21 orifice) sampling probe was manufactured and placed into the hot exhaust flow outside of the exhaust nozzle. From the probe inlet, three meters of 12 mm Internal Diameter (ID) stainless steel tube was used to transport the emissions sample to a Dekati eDiluter Pro. The eDiluter used ejector diluter principles and incorporates two-stage dilution with a control system to achieve adjustable high dilution ratios. For this experiment, the eDiluter was operated at 25:1 dilution ratio using compressed and filtered ambient air generated by an onsite oil free compressor filtered through a HEPA filter. Four test fuels were used, namely: JetA-1 fuel purchased at the airport (referred to as JetA-1 source.1), 50% HEFA based SAF mixed with JetA-1 source.1 purchased at the airport (referred to as SAF blend.1), Neste supplied JetA-1 (referred to as JetA-1 source.2), and Neste supplied 50% HEFA based SAF premixed with JetA-1 source.2 (referred to as SAF blend.2).

The test points used for the emissions testing of the 502 and 507 engines were determined prior to full emissions testing to be representative of the ICAO Landing Take-Off (LTO) cycle power conditions (ICAO 2017). They were determined by empirically assessing the measured unburnt hydrocarbons (UHC), carbon monoxide (CO), and nitrous oxides (NO_x) Emission Indices across a ten-test point up and down power curve. Corresponding engine power conditions (quantified by the reported engine T30 temperatures – temperature before the inlet of the combustor) were then used to define repeatable engine performance points across the different fuels and ambient conditions tested. Note that it was observed that for the approach-type condition, two T30 temperatures were required to match NO_x and CO reported in the ICAO databank, which was thought to be attributed to a bleed switch point.

In total, eight engine powers were tested ranging from ground idle, the minimum achievable power on a given day (circa 4% power), to the maximum take-off (circa 100% power) – with idle (5%), taxi (7%), approach (30%), approach max NO_x (40%), cruise (70%), and climb (85%) in-between. The test points were sequentially conducted as part of an up-curve and down-curve thrust driveline cycle, with some repeat test points on both curves, namely; idle, taxi, approach, cruise, and climb. Several engine parameters were measured for each test point, for this study, the key reported parameters are normalized power and the exhaust temperature. The normalized engine power was the percentage of the maximum power that could be produced by the engine; note that due to some engine degradation, 100% power quoted from the engine manufacturer for a new engine was not possible. The exhaust temperature was deemed the most appropriate parameter to correlate to the measured charge of the emissions, as it is generally assumed to correlate to flame temperature (Latarche 2021; Lee 2013), which is thought to be a main driver of the charge of the emissions (Fialkov 1997; Calcote 1962). The different test points (denoted by makers in Figure 2) used for each fuel and engine for the exhaust temperatures are shown in Figure 2. As would be expected, the exhaust temperature were observed to increase with an increase in normalized power. However, as seen the increase in the three parameters was not perfectly linear, with some step changes, most notably for the last three power conditions used for the 507. Additionally, there were no significant changes in the temperatures across the different fuels used. There were some minor differences in exhaust

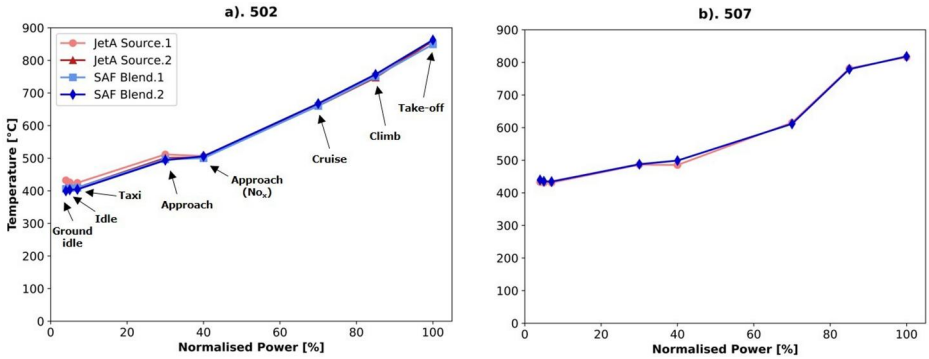

Figure 2. Test points, as a function of normalized power, used for the (a) 502 and (b) 507 engines with the associated LTO-like condition annotated and denoted by the markers for both the exhaust temperatures. Note that the order of the LTO test points indicated by the markers for the 502 engine (a) are the same for the 507 engine (b).

temperatures noted between some of the repeated up-cycle and down-cycle test points – up to 20 °C (0.05%) for the idle, taxi, and approach test points. A full breakdown of the exact exhaust for both engines can be found in the SI.

2.3. Gnome turboshaft helicopter engine experiment

The Gnome turboshaft helicopter engine was tested at a Rolls-Royce engine test facility in Derby (UK) over a week test period in February 2023. The engine was the same as tested in previous emission studies by Olfert et al. (2017) and Smith et al. (2022), thus further details about the engine can be found in these publications. The Gnome engine was operated at two power conditions, namely; low power (13,000 RPM; idle-type) and high power (22,000 RPM, near take-off), using JetA-1 supplied from the Rolls-Royce onsite fuel farm (referred to as JetA-1 source.3).

The emissions probe consisted of a single point open-faced 8 mm ID stainless steel sample probe placed into the direction of the engine exhaust flow. After the inlet of the probe, the stainless steel tube was bent 90°, followed by a 1 m straight length, before entering a sharp-cut cyclone used to remove large particles (above 1 µm). As seen in Figure 1, from the cyclone, the sample was diluted with particle-free zero grade nitrogen at a dilution ratio of 8:1 using a Dekati Di-1000 ejector diluter. Before the diluter, the sampling temperature was maintained at 160 °C to minimize the effect of thermophoretic losses and to supress water condensation within the sampling system. From the diluter, the sample transferred into an expansion plenum, where the flow velocity was reduced, before being sampled *via* a 1/4" ID stainless steel inlet probe perpendicularly entering the plenum and bent through 90° to face into the flow. The probe from the plenum was connected to the measurement instrumentation using a 2 m long, 1/4" ID conductive silicone tube.

2.4. Instrument calibration, inter-comparison, and cleanliness

To ensure that the measurements were consistent across all test points and periods, a rigorous calibration and inter-comparison procedure was completed before any measurements were conducted. Pre-experiment tests, akin to those outlined in Kittelson et al. (2021) and Wiedensohler et al. (2018), were conducted before each test campaign to validate the measurements from the SMPS, CPCs, and electrometer. All flow were conducted by using a Sensidyne Gilian Gilibrator 2-USB Calibrator and all zero-particle checks were conducted by using a HEPA filter. The checks included inter-comparing the two CPCs that would be used for measurement in terms of output number concentrations at designated particle sizes, inlet flow, and zero-particle checks. The SMPS was inter-compared against another SMPS, and was flow checked, zero-particle checked, pressure checked, and size-calibrated using 51, 92, and 152 nm polystyrene latex spheres (PSL). The electrometer flow was checked and any electrical current offset was corrected for using zero-particle air and an ESP turned on to remove all charged particles to determine a true zero, thus accounting for possible systematic errors and instrument drift. Note that the offset is typically corrected within the instrument software prior to testing; however, the authors undertook regular measurements of the offset throughout the test campaigns facilitating a post-test correction of the electrometer data.

The ratio between the measured concentrations of the CPCs (particle sizes ranged from 7.5–150 nm) was between 0.7–1 – note that above 10 nm the ratio was between 0.8–1. Although for the 502 and 507 engine

tests, the ratio was between 0.92–1 following a service and calibration from the manufacturer. The SMPS particle size classifications against PSLs over-reported by 4–8% across all campaigns, which was accounted for by using a delay time correction (*Td*) of 1 s as recommend by TSI (2016), which was used to subsequently corrected for all particle size distributions throughout the campaigns. For this correction, essentially the particle size distributions were shifted to account for differences in particle residence times between the DMA and CPC. An example of original and corrected particle sizes distributions using the PSLs are shown in the SI. The measured electrometer current offset across the test campaigns was between 10–27 fA with a standard deviation of less than 1 fA. As mentioned, the offset was not changed within the electrometer software, neither at the beginning or across each campaign, thus although a current offset seems fairly large, this was not considered to cause significant inaccuracies or uncertainties for the measurements given the offset mainly represented the instrument drift between each campaign.

In addition to the pretest calibrations, all instruments were checked throughout the test periods. For the CPCs, at the beginning of each day, a zero-particle check was performed along with intermittent inter-comparisons of particle number concentration across a range of particle sizes. The SMPS was also zero-particle checked at the beginning of each day and intermittently size-checked using PSL particles.

Although the charge generated through each element of the sampling system was not fully characterized, it was assumed that this would not have a significant impact on the charge compared to that generated by the aircraft engine. However, it should be noted that this may have caused some uncertainties in the final charge measurements, which have to be considered when analyzing the results - this will be covered in more detail in Section 3. This being said, a fairly simple check was conducted by measuring the electrometer electrical current produced from ambient air passing through the sampling system from the inlet of the diluters while the ESP was upstream of the diluter and turned on and turned off- the full details of this check can be seen in the SI. The results showed that no excess difference in charge occurred between ESP turned on and turned off.

3. Results and discussion

The results are divided into two sections, namely: Section 1: charge measurements of the Honeywell ALF502 (502) and LF507 (507) turbofan engines and Section 2: charge measurements of the Gnome turboshaft helicopter engine. In each section, the particle size distributions are initially presented, which are subsequently used to determine the charged fraction as a function of particle diameter. The total charged fraction measurements of the different engines emissions are then introduced along with the mean charge per particles, either as figures in the case of the 502 and 507 engines for the numerous power conditions and fuels tested, or in a table for the Gnome given the limited number of power conditions tested.

All error bars in the figures represent the uncertainty in the measurements determined from the instrument stability, which was calculated based on the process outlined in Section 2.1. Note that there was no data for the 507 engine using JetA-1 source.1 due to instrument data recording issues occurring for this test.

3.1. Charge measurements of honeywell ALF502 (502) and LF507 (507) turbofan engines

The following results first show the effects of engine power (corrected to exhaust temperature based on Figure 2) on the particle size distributions. The Geometric Mean Diameter (GMD) of the distributions are then used to summarize the effects of engine power and fuel composition on the emissions. The GMDs, total particle concentrations, and particle size distributions are used to determine the charged fractions. Then the measured total particle concentrations and the electrical current produced by the emissions is used to give the mean charge per particle. As discussed previously, both the charged fraction and mean charge per particle, when considered together, give an indication as to the amount and polarity of the charge carried by the emissions.

The particle size distributions presented below correspond to sampling with the ESP turned off, including all charged and uncharged emissions. Note these distributions are only a subset of the engine powers and fuels measured, namely; approach (30% power) test points and take-off (100% power) test points when using JetA-1 source.1 and SAF blend.1 for both the 502 and 507 engines. As discussed previously, in Section 2.3, the reader is reminded that for Figure 3, the nano DMA was used to measure the particle size distributions for the 507 engine while the long DMA was used for the 502 engine, hence the different particle size ranges. In addition to the approach and take-off test points, the distributions between these

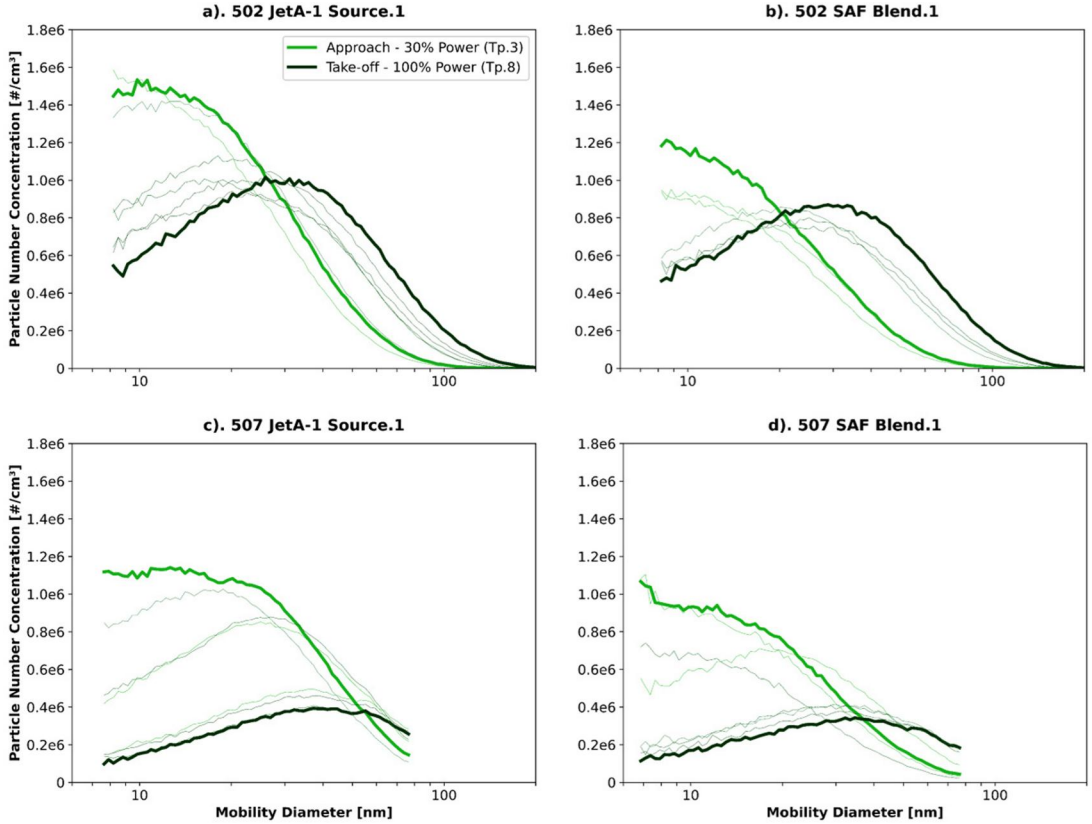

Figure 3. Engine emissions particle size distributions for approach (30% power) and take-off (100% power) test points for (a) 502 engine using JetA-1 source.1, (b) 502 engine using SAF blend.1, (c) 507 engine using JetA-1 source.1, and (d) 507 engine using SAF blend.1. The size distributions for the intermediate test points are also included and represented by the fainter lines. Note the difference in the location of the start and end of the distributions, which was due to the nano DMA being used to measure the 507 engine emissions particle size distributions while the long DMA was used for the 502 engine emissions particle size distributions.

test points are included in the figures and shown by fainter lines. The distributions for the test points below the approach (ground idle and taxi) are not included as a sub-10 nm peak was observed that was thought to be due to volatile particles or UHC nucleating in the eDiluter. To be as representative as possible of the emissions at the engine exhaust, this peak was removed by fitting a lognormal distribution to the dominant (nvPM) mode to determine the GMD for analysis later in this section – refer to the SI for a description of the procedure used. The complete set of particle size distributions for both engines using JetA-1 source.2 and SAF blend.2 are shown in the SI.

By comparing the particle size distributions produced by the approach and take-off test points in Figure 3, three qualitative trends were observed as the power of the 502 and 507 engines increased: an increase in particle size, a decrease in particle concentration, and a broadening of the distributions. All three of these trends are in agreement with the published literature (Corbin et al. 2022; Durdina et al. 2024; Lobo et al. 2015), and are attributed to an increase in the primary particle size and the amount of particle aggregation with power (Durdina et al. 2014; Hu et al. 2022; Kinsey et al. 2011). Similarly, the SAF blends also produced a lower particle number concentration, in agreement with several published studies (Durand et al. 2021; Durdina et al. 2021; Teoh et al. 2022; Xu et al. 2024). A similar trend was observed for the JetA-1 source.1 and SAF blend.2 shown in the SI. Comparing the particle size distributions produced by each of the engines shows that for the approach and take-off engine power, the 507 engine produced lower particle number concentrations than the 502 engine at similar powers and fuels, particularly evident for the take-off power.

To summarize, a quantitative comparison of all the particle size distributions measured for the 502 and 507 engines, for the four fuels across the eight engine powers, the derived GMDs are plotted against exhaust temperature, shown in Figure 4.

As would be expected and in agreement with the conclusions drawn from Figure 3, as the engine power increased (shown by an increase in exhaust

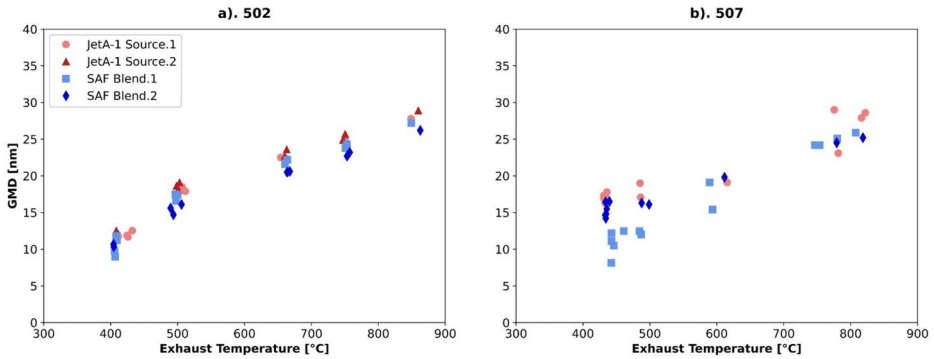

Figure 4. Measured particle size distributions GMDs for all four fuels and engine powers as a function of exhaust temperature for the (a) 502 engine and (b) 507 engine. No error bars are included as for some of the particle size distributions only one scan was taken – see the discussion in Section 2.3. Note the missing data for the 507 engine using JetA-1 source.2 due to instrument data recording issues occurring.

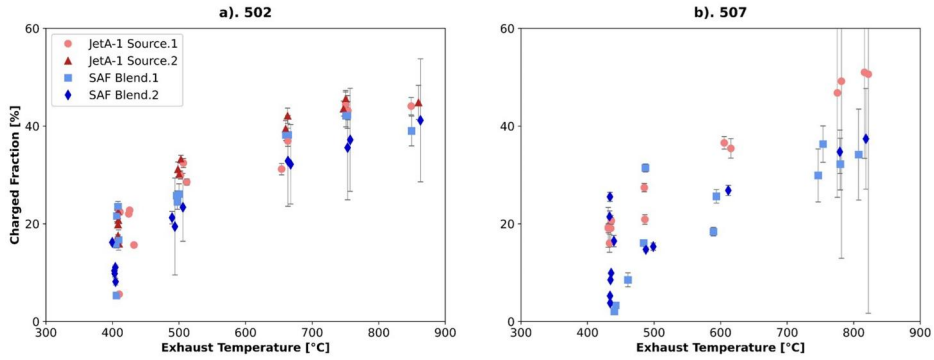

Figure 5. Total charged fraction for each fuel and engine power test point used as a function of the exhaust temperature for (a) 502 engine and (b) 507 engine.

temperature) the GMDs increased from ~10nm at an exhaust temperature of ~400 °C (ground idle) up to ~27nm at ~860 °C (take-off), shown in Figure 4. The observed trend shows an almost linear increase, which was repeatable across the different fuels tested. Comparing the GMDs of both engines using JetA-1 and SAF revealed a decrease of a few nano meters in the GMD for SAF, indicating that SAF generates smaller particles, consistent with findings from the literature stated above. When comparing the two engines, it was observed that the 507 engine produced particle size distributions with GMDs that were more scattered. Although a conclusive reason for the scatter has not be determined, it should be noted that the 507 engine had some stability issues, where the engine had to be shut down and restarted, along with some test points conducted when it was raining. However, the scatter could also be a result of estimating the GMD from a particle size distribution that was not fully closed, which was not as much of an issue for the 502 engine due to the use of a different DMA (long DMA) that was slightly better at measuring more of the particle size distributions. Alternatively, the scatter, for low power test points, could have been caused by fitting process used to remove volatiles peak, although the same process was used for the 502 engine where the same scatter was not observed.

For each GMD measured from the aircraft engine emissions shown in Figure 4, the total charged fractions of the emissions was investigated by comparing the difference in particle concentration when the ESP was turned on and turned off. For both the 502 and 507 engines, the total charged fractions are plotted as a function of the engine exhaust temperature in Figure 5 and GMDs in Figure 6, enabling comparison of the respective trends.

From Figure 5, it was observed that there was a dependence of total charged fraction on the aircraft engine emissions as a function of exhaust temperature - as the exhaust temperature increased so did the total charged fractions for both engines across all fuels tested. One explanation, which has been proposed from numerous studies (Lukachko et al. 1998; Sorokin et al. 2003; Starik 2008), was that as the flame and post-flame temperatures (here the exhaust temperature was used as a proxy) increases the ion production rate

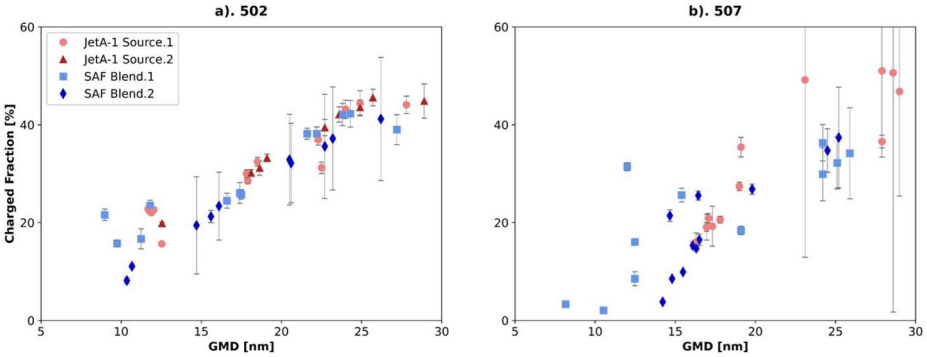

Figure 6. Total charged fraction for each fuel and engine power used as a function of the particle size distribution GMD for (a) 502 engine and (b) 507 engine.

increases, resulting in the production of more charged particles.

One further finding from Figure 5, a clear fuel dependence was observed, where generally for all exhaust temperatures using the SAFs produced a lower total charged fraction compared to using the JetA-1 – on average over all exhaust temperatures of 11% for the 502 and 17% for the 507 engine.

However, from Figure 4, it was observed that as the engine power increased, so did the particle size (represented by GMD). It is well established that as particle size increases, so does the charge carrying capability and probability (Gunn 1955; Wiedensohler 1988). Therefore, this may also cause the resulting increase in total charged fraction. In addition, an increase in particle size was also observed for the JetA-1 compared to the SAFs, which may be the cause of the increase in total charged fraction of JetA-1 compared to SAF. Thus, the total charged fraction as a function of GMD was plotted in Figure 6 to assess the dependence of GMD on total charged fraction.

In Figure 6, the increase in total charged fraction as particle size increases, as discussed above, can be observed, confirming that as the particle size increased so did the total charged fraction. The trend appears to be almost linear for the 502 engine (R^2 value of 0.8873), but more scattered for the 507 engine (R^2 value of 0.7932). Although it appears that the driving parameter of total charged fraction of the emissions was due to particle size, as the total charged fraction as a function of GMD in Figure 6 showed a near linear increase, the effect of additional ion generation as the engine power increased cannot be completely discredited as causing the increase in total charged fraction.

In terms of the fuel dependence on the total charged fractions shown in Figure 5, this could be due to several reasons, but is likely due to the particle size rather than fuel composition. Therefore, from the results presented, an indirect dependence on total charged fraction can be proposed, due to associated increase in particle size of the emissions when using JetA-1 compared to SAF.

To interrogate the aforementioned driving parameters further, a charged fraction as a function of particle diameter was determined, shown in Figure 7. This was determined by using the particle size distributions presented in Figure 3, along with the size particle distributions for the uncharged particles, measured when the ESP was turned on. This allowed a general analysis of the charged fractions across the different particle size distributions mobility diameters for both engines, fuels, and engine powers (exhaust temperatures) to be conducted. Thus, providing a means of all three parameters discussed in Figures 4–6 to be analyzed. Similar to Figure 3, the measurement from two test points are highlighted, with the measurements from intermediate test points included with lighter lines for completeness. For Figure 7, the ground idle (4% power) test point was used instead of the approach as the 'volatile' peak observed below 10 nm was assumed to cancel-out through the division process used to determine charged fraction, so having no impact on the reported charged fractions, as particles at this size are thought not to carry much charge. However, to mitigate any confusion, the charged fractions as a function of particle diameter plots have been cropped below 10 nm – an example plot over the full range can be found in the SI. Note the approach test point is included in the figure, but as a fainter line, along with all other test points.

As found for Figure 6, the charged fractions as a function of particle diameter shown in Figure 7, across the particle size distributions mobility diameters was observed to increase as the particle size increased (mobility diameter used as a proxy for

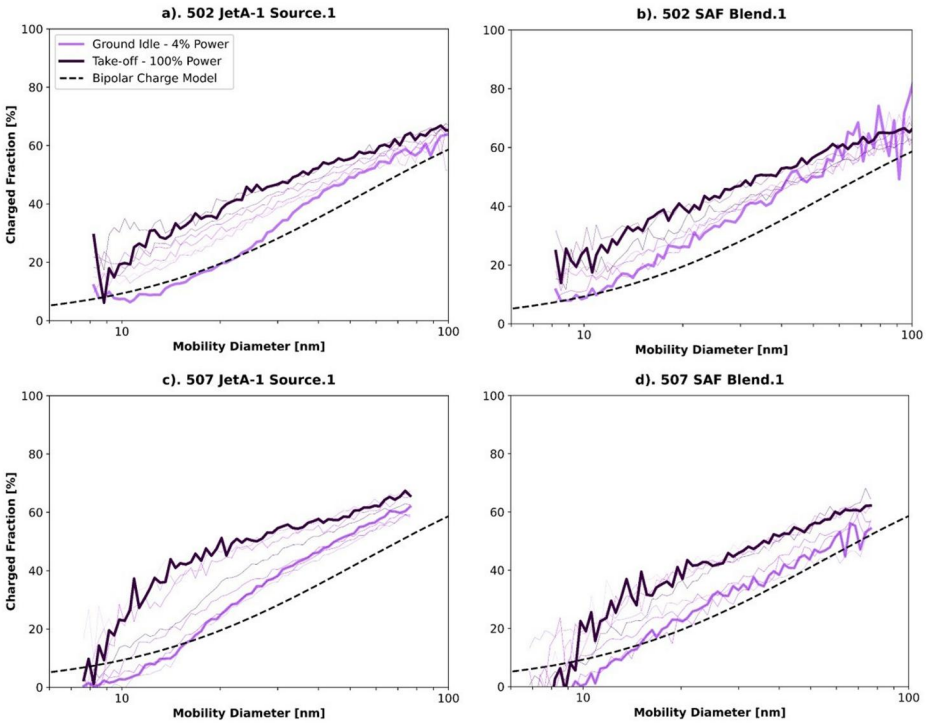

Figure 7. Charged fraction as a function of particle diameter for ground idle (4% power) and take-off (100% power) engine condition test points for (a) 502 engine using JetA-1 source.1, (b) 502 engine using SAF blend.1, (c) 507 engine using JetA-1 source.1, and (d) 507 engine using SAF blend.1. The charged fractions for the intermediate test points are also included, represented by the fainter lines. The (black) dashed line represents the predicted charged fraction from a symmetrical bipolar charge distribution.

particle size), between 7–33% charged at 10 nm increasing to 55–71% for 80 nm across both engines and fuels. Furthermore, there was a clear increase in charged fractions as a function of particle diameter as the engine power (exhaust and flame temperature) increased. Therefore, it can be inferred that both processes, increase of GMD and increase of ion production with increasing engine power caused an increase in the charged fractions of the emissions.

In addition to this main conclusion, comparing the measured particle charged fractions against the predicted charged fraction from the bipolar aerosol charge model (dashed line), shows that the engines at take-off generated more charged particles than a typical symmetrical bipolar charging processes at ambient conditions. Although the agreement with the model prediction for the ground idle test points suggests that the two engines did produce charged fractions similar to that of an symmetrical bipolar charging processes – with some over prediction of the model at the smaller particle size, particularly evident for the 507 engine. Note the high variability in the charged fraction as a function of particle diameter curve for the 502 engine using SAF blend.1 above 60 nm for the ground idle test point, which was due to the low particle concentrations above 60 nm (see Figure 3b).

In terms of fuel composition dependencies, there was no perceivable difference observed for the charged fractions as a function of particle diameter shown in Figure 7 within the measurement uncertainty. In terms of different engines, similar charged fractions as a function of particle diameter for particle sizes above 20 nm were observed. However, there was slightly different trends for sub-20 nm particle sizes. For the 507 engine as the power increased, there was a clear shoulder present in the curves at the smaller particle size ranges (between 10–20 nm). This indicated that the 507 engine produced more charged particles (8–13%) between 10–20 nm compared to the 502 engine. Although for smaller particles, when at idle power, the charged fraction as a function of particle diameter of the 507 engine drops compared to the 502 engine.

However, it should be noted when considering the differences between the charged fractions as a function of particle diameter between the two engines, two slightly different experimental set-ups were used – the long DMA was used to measure the 502 engine while the nano DMA was used to measure the 507 engine. This may have resulted in some measurement difference. In addition, the methodology of using an SMPS to determine the charged fractions as a function of particle diameter depends on the multiple charge

correction used for the SMPS inversion being correct, this is particularly important for the smaller particles in the measured distributions from the SMPS. Some authors (Chen and Jiang 2018; Leppa et al. 2017; Nishida et al. 2025) have found that this correction is not necessarily correct in every use-case even in standard configurations, and thus this may have caused some inaccuracies in the charged fractions as a function of particle diameter results shown in Figure 7.

As discussed, although the charged fractions measured and discussed above provide information on the proportion of the aircraft engine emissions that were charged, they offer no insight into the polarity of the charge the emissions carried. Therefore, an electrometer (measuring electrical currents), combined with the particle number concentrations, was used to determine the overall polarity and mean charge per particle of the emissions produced for each engine power investigated. The results are shown in Figure 8 for both the 502 and 507 engines, across different engine powers (indicated by exhaust temperatures), and fuels. Note that given the mean charge per particle presented here is based on the total particle concentration and the overall electrical current reported by the electrometer, the values reflect the mean bias, or net, of all of the emissions toward a given charge polarity, rather than the true mean charge per particle of individual particles in the emissions sample. For example, if the mean charge per particle is zero, this reflects that either no charge was present on the emissions sample or the emissions sample carried a completely symmetrical bipolar charge distribution, so that positive and negative charged emissions cancel each other. Furthermore, the results discussed below represent the mean charge per particle of the total emissions sampled at the measurement location, which may include solid particles, semi-volatiles, volatiles, and ions.

Starting with the mean charge per particle of the emissions produced by the 502 engines (Figure 8a), a clear trend of increasing mean charge per particle with exhaust temperature toward a positive bias of up to 0.08 charges per particle was observed starting between ~500 °C (approach) and ~650 °C (cruise). This indicates that the charge distribution of the emissions at the sampling location for this engine was asymmetrical with more positive charge overall. It is difficult to determine what the exact charge distribution of the emissions was as the exhaust temperature increased; however, as indicated in previous studies (Sorokin and Arnold 2004) both negative and positive ions have been reported in the exhaust plume. Therefore, it was assumed that the charge distributions of the emissions are bipolar with a bias toward positive charge. As discussed earlier, this trend toward a positive polarity bias could be explained by the increase in post-flame thermal ionization, as theoretically predicted from in the literature (Sorokin and Arnold 2004; Vatazhin et al. 2004). For the exhaust temperatures below ~500 °C (approach, taxi, idle, etc …), the mean charge per particle of the emissions reduced to near zero. Although this may imply that there was no charge on the emissions at these test points, it was more likely that the charge distributions were symmetrically bipolar, consistent with other lower temperature/pressure combustion systems, due to the fact that a charged fraction was observed (Figures 5–7) for these test points, this trend is also predicted by the literature.

However, it cannot be fully discounted that the charge of the emissions was effected by the sampling system components, such as the tubing, diluter, and even some potential ESP current flows, either from

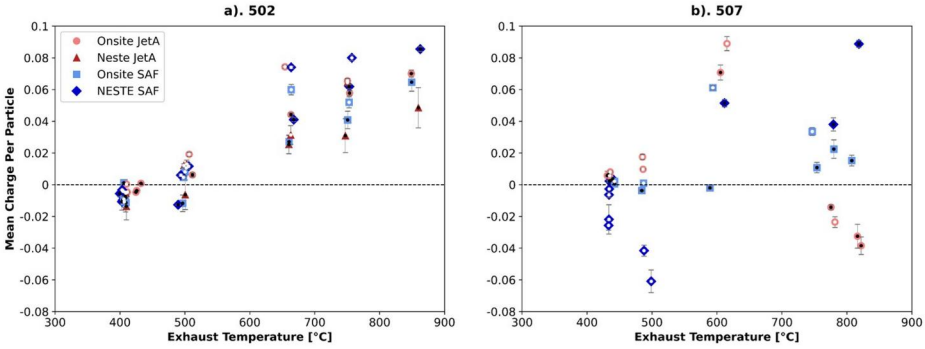

Figure 8. Mean charge per particle of the aircraft emissions for each fuel and engine power as a function of exhaust temperature for the (a) 502 engine and (b) 507 engine. The markers with the black dots inside represent the up-cycle engine powertrain test points while the marker with the white dots inside represent the down-cycle engine powertrain test points. The dashed black line represents the location at which zero mean charge per particle bias occurred.

charge-dependent losses (Lidstone-Lane et al. 2025), unsteady charging dynamics through the tubes (Johnson et al. 2020; Nishida et al. 2025), unaccounted-for component charging effects. Although various attempts were made to mitigate these effects, such as keeping all tubing as short as possible, only using stainless steel tubing, and characterizing the diluter to determine that it caused no excessive charging, due to the complexity of measuring aircraft emissions, some of the effects could still have impacted the charge of the measured emissions. Nevertheless, out of the three effects, it was thought that the main source of uncertainty was due to the unsteady charging through the tubes. This effect has been found in some studies (Nishida et al. 2025) where ions in the post-charging process flow have been reported to continue to effect the charge distribution, particularly as negative ions with higher mobility are more easily lost to the walls compared to positive ions. Although the unsteady charging through the tubes for the aforementioned study only considered much shorter tubing lengths (<0.33 m) compared to the tubing used in this study (>2.5 m), which may mean this effect was not as prevalent. Yet, due to these dynamical effects, it cannot be assumed that the measured charge distributions are completely representative of the aircraft engine emissions at exhaust exit (sampling system inlet). Therefore, caution should be applied when interpreting exact values from the measurements, and the uncertainties the unsteady charge related effect may cause, should be considered.

In terms of different fuels, there was some minor evidence that the fuel composition had an effect on the mean charge per particle of the emissions produced by the 502 engine. Most notably, the SAF blend.2 had a slightly larger mean charge per particle than the rest of the fuels for each test point above 650 °C, by up to 0.016. However, due to the scatter observed, this may just have been due to the uncertainty in the measurement.

For the 507 engine (Figure 8b), a large amount of scatter was observed across the different fuels and test points, thus it is difficult to attribute a conclusive trend to the mean charge per particle data. Although these measurements are thought to be potentially erroneous, it may be that these results are true and the 507 engine produces charged emissions carrying variable polarities for the same up-cycle then down-cycle test points, unlike the clear trends observed from 502 engine. However, variability of the mean charge per particle measurements was difficult to ignore, particularly when considering the opposite trends across similar fuels (SAF) – relatively high negative mean charge per particle measurements for low engine power conditions (<500 °C) for the SAF blend.2 compared to the SAF blend.1. In addition, the trend observed for the JetA-1 compared to the SAF, which would show that there was a significant fuel composition dependence on the mean charge per particle (high engine power causing negative emissions for JetA-1, but positive emissions for SAF). Conversely, only minor fuel composition dependence was observed for the 502 engine, which did not include a polarity change. As both used essentially the same sampling system, and the engine technologies were very similar, the uncertainties due to unsteady charging, discussed above, was unlikely the main cause. More likely, was that it was due to the engine stability and weather conditions mentioned above. This becomes more apparent when considering that the engine stability and weather issues occurred for the potentially erroneous test points discussed. For the SAF blend.2 test, it started to rain halfway through the test, for the down-cycle points (blue diamonds with white dots) from approach to ground idle (sub-500 °C temperature). This may have meant that large amounts of water was entrained into the engine for only these test points. For the JetA-1 source.1 test, the engine had to be shut down and restarted several times. Nevertheless, to confirm either way, and rule out the weather and engine stability effect, more data for dry and stable engine operation is required.

3.2. Charge measurements of Gnome turboshaft helicopter engine

In addition to the 502 and 507 engines, the charge of the emissions produced from the Gnome engine was measured for two engine powers using onsite (supplied from Rolls-Royce fuel farm) JetA-1 (JetA-1 source.3). Similar to above, the particle size distributions and charged fraction as a function of particle diameter were measured and are presented in Figure 9 below. The total charged fractions and mean charge per particle were also measured and are shown in Table 1, along with the key emissions parameters relating to charge measurement methodology used for this study. Some comparison will be drawn between the Gnome engine and the 502 and 507 engines; however, it should be noted that these are different engine technologies that were measured with different sampling systems.

From the particle size distributions shown in Figure 9a, the Gnome engine was observed to produce

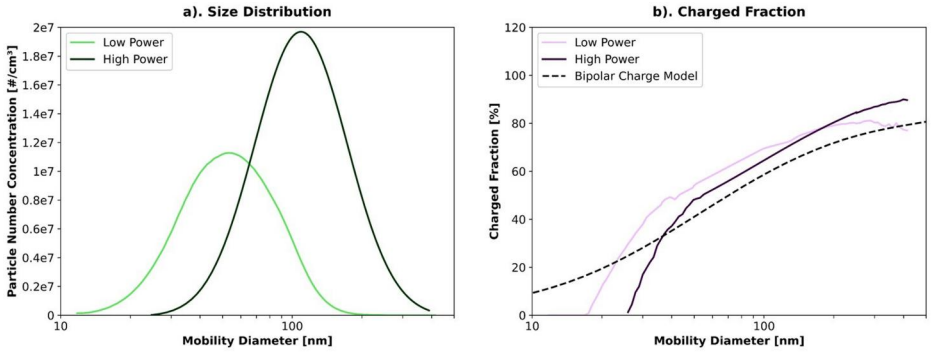

Figure 9. Gnome emissions produced when using JetA-1 for two engine powers (low power ∼ near idle and high power ∼ near take-off), where (a) particle size distributions and (b) charged fractions as a function of particle size. The (black) dashed line in (b) represents the predicted charged fraction from an equilibrium bipolar charge distribution.

Table 1. Charge parameter results for the two engine conditions used for the Gnome engine along with the particle concentrations and particle size distribution GMD.

Power	Particle concentration (particles/cm^3)	GMD (nm)	Total charged fraction (%)	Mean charge per particle
Low	5.99e^6	45.0	50.6	−0.091
High	7.45e^6	105.1	58.1	0.013

larger particles than both the 502 and 507 engines with GMDs of 45 nm at low power and 105 nm at high power (compared to the 502 and 507 engines which produced <20 nm for idle and <30 nm for take-off). In addition, from Table 1, the measured particle number concentration were significantly larger for the Gnome engine compared to the 502 and 507 engines (5.99e6 particles/cm^3 at low power and 7.45e6 particles/cm^3 at high power). Although, note that this could be largely attributed to the different sampling systems used, specifically the diluters – less dilution was used (25:1 for the 502 and 507 while 8:1 was used for the Gnome engine). This being said, the charged fraction as a function of particle diameter did show the same general trend across the mobility diameters as was observed for the 502 and 507 engines; namely that as the particle size increased so did the charged fraction. Unlike the 502 and 507 engines, the Gnome engine produced particles up to 350 nm, which resulted in charged fraction of up to nearly 90% for the larger particle size produced by the Gnome engine, thus further supporting the hypothesis of increasing charged fraction with increasing particle size.

For the Gnome engine, between the two engine powers, for particles above ∼40 nm, the charged fractions as a function of particle diameter did not differ significantly from each other or from the bipolar charge model. Below 50 nm, the charged fraction dropped to near-zero. A similar trend was observed for the 507 engine (Figures 7c and d), and although no conclusive reason for this sudden drop off is given, this could be due to the instrument artifacts discussed for the 507 engine. However, this could also be an indication that charge-dependent particle losses, particularly electrostatic dispersion, occurred. This additional point is discussed for the Gnome engine but not the 507 engine, as the Gnome engine generated particle concentrations were well into the threshold (>1e6 particles/cm^3) for electrostatic dispersion to occur (Malendari et al. 1975; Fialkov 1997) – see Table 1 for the total concentrations. This theory is supported further as electrostatic dispersion is known to more readily effect small charged particles with high mobility (Kasper 1981; Virtanen et al. 2001). However, the reduction in charged fraction for the smaller particle sizes could also be explained by enhanced charge assisted coagulation, due to the large emissions concentrations (Fialkov 1997), which would affect the full particle size distribution and charged fraction as a function of particle diameter. Due to the unknowns, to confidently attribute a mechanism that caused the drop in charged fraction as a function of particle diameter at the smaller particle size ranges, for both the Gnome and 507 engines, more measurements would need to be conducted.

To investigate the charge of the emissions produced by the Gnome engine further, several key parameters are shown in Table 1. These parameters include the total particle concentrations of the emissions, the GMD of the particle size distributions, the total charged fractions, and the mean charge per particle.

For the Gnome engine, in agreement with the observations for the 502 and 507 engines, the total charged fraction of the emissions increased with engine power, as see in Table 1. Although the total

charged fractions of the emissions was larger for the Gnome compared to the 502 and 507 engines (largest charged fraction for the Gnome was 58.1% compared the largest of the 502 or 507 engines, which was 51% for the 507 at take-off). As was found above, the charged fraction was dependent on GMD, which is clearly shown in Table 1, with an increase in charged fraction as the GMD increased from 45 nm (low power) to 105.1 nm (high power).

The magnitude of the mean charge per particle of the emissions produced by the Gnome engine decreased (from 0.091 to 0.013), tending to a symmetrical bipolar charge. This being said, the polarity flip from negative to positive as the engine power increased was the same trend as that observed in the 502 and 507 engines (apart from when the 507 was using JetA-1 source.1) and predicted in the literature. It is unclear what caused the trend in mean charge per particle magnitude of the Gnome engine compared to the 502 and 507 engines, but could be due to several reasons. Firstly, the difference in engine technologies between the Gnome engine and the 502 and 507 engines, the Gnome is a turboshaft engines whereas the 502 and 507 engines were turbofan engines. Also, the sampling system to measure the emissions were different, with longer residence times expected for the Gnome engine sampling system compared to the 502 and 507 engines, which may cause addition unsteady charging dynamics to occur, rendering the charge of emissions measured for the Gnome less representative of engine exit compared to the 502 and 507 engines. Furthermore, as mentioned above, the larger particle concentration measured for the Gnome engine compared to the 502 and 507 engine may have resulted in additional charge related effects; for example, charge-assisted coagulation.

4. Conclusion

The charge, including the charged fraction and mean charge per particle, was experimentally measured for aircraft exhaust emissions produced from three engines: a Honeywell AFL502 (502) turbofan, Honeywell LF507 (507) turbofan, and a Gnome turboshaft helicopter engine. The dependence of engine power (or exhaust temperature and used as a proxy for flame temperature), GMD, and fuel composition (JetA-1 and 50% blended HEFA and JetA-1, referred to as SAF) on the charge of the emissions was investigated to determine the key parameters driving the charge. Understanding the charge of aircraft emissions has many important implications, including feeding into contrail modeling approaches, better determining the implications of aircraft emissions on human health, and providing better accuracy of aircraft emissions sampling leading to more robust reporting.

This study empirically supports findings that the aircraft emissions carry a charge that increases with engine power (exhaust temperature), which was observed for all three engines; for example, taking the Gnome engine, 50.6% of the emissions were charged for low power while 58.1% of the emissions were charged for the high power. The increase in charge was attributed to three factors: larger particles generated which could carry more charge, more ions generated as the engine power increases, and higher post-flame temperatures causing thermal ionization. Although it was not fully determined which parameter was key to driving which aspect of the charge, it was thought that all three had an impact. The most easily discernible parameter, and the most likely to drive the overall charged fraction, was the increase in particle size as engine power increased. A clear trend was found across all engines and fuels tested that as the GMD increased so did charged fractions. For the other two parameters, it was more difficult to confidently discern that they effected the charge, as the associated increase in these parameters (engine power) also increased the particle size. However, using the charged fraction as a function of particle diameter, it became evident that as the engine power increased, the charged fraction increased across all mobility diameters (a measure of particle size) of the particle distribution, suggesting that particle size was not the only driving parameter. In addition, using the mean charge per particle (notably for the 502 engine), a clear increase toward positive polarity of the bias or net charge as engine power increased was observed, which is predicted from literature to be due to an increase in post-flame thermal ionization. Although some effects may be due to the differences in mobility of the different polarity ions through the sampling systems.

In terms of the dependence of the charge due to the different fuels, there was a difference in charge observed; namely, that the JetA-1 produced more charged particles for all engine powers compared to the SAF – on average 11% across the engine powers for the 502 engine and 17% for the 507 engine. Suggesting that there was a fuel dependence on the charge of the emissions, which was mainly attributed to the difference in particle size of the emissions produced by each fuels – larger particles from the JetA-1 compared to the SAFs. For the 502 engine, the SAF

showed a slightly larger mean charge compared to the JetA-1, although the significant scatter across the test points of the four fuels meant a confident trend could not be attributed. For the 507 engine, a completely different trend was observed, where the larger engine powers (high exhaust temperatures) the SAF produced a positive polarity and JetA-1 produced a negative polarity. For the trend of the 507 engine, it could not be discounted that engine stability issues that caused the engine to be restarted several times while using JetA-1 resulted in inaccuracies rendering these results inconclusive. Thus, for a confident conclusion to be drawn for the fuel effects on the mean charge per particle measurements, particularly for the trend observed for the 507 engine, more data is required.

For all of the observed trends, a number of uncertainties that may have affected the conclusions were determined. The most significant uncertainty regarded the representativeness of the measured emission to that of those that would occur at the aircraft engine exhaust exit. A change in representativeness may have occurred due to unsteady continuous charging and ion dynamical effects arising through the sampling system that were not accounted for. These uncertainties would more significantly impact the comparison of the 502 and 507 engines to the Gnome engine datasets given the sampling set-up were different. Considering the comparison between these two set-ups indicated that a sampling system that results in the emissions having longer residence times, as can be assumed for the sampling system used for the Gnome engine, could results in more unsteady charging occurring rendering the measured emissions even less representative of the aircraft engine exhaust exit, in terms of charge. Therefore, this may mean that detailed charge characterization of the sampling system would be required to ensure that the measured emissions at the measurement location is fully representative of the aircraft engine exhaust exit.

Acknowledgements

The authors would like the acknowledge the National Centre for Atmospheric Science's (NCAS) Atmospheric Measurement and Observation Facility (AMOF) for use of the SMPS, electrometer, and CPC used in this project. The authors would also like to acknowledge CFS Aero Parts for operating the engine and support with the test facility, Neste for supplying some of the fuel that was used for the 502 and 507 engines, and NRC Canada (Greg Smallwood, Rym Mehri, and Brett Smith) for allowing some measurements to be taken on their Gnome campaign.

Disclosure statement

No potential conflict of interest was reported by the author(s).

Funding

The project was funded by a PhD studentship through ESPRC Center for Doctoral Training in Aerosol Science EP/S023592/12440391, and co-sponsored by Rolls Royce Plc. The experimental programme received funding from NERC's decarbonization initiative and SAMPLE IV (Grant agreement No: MOVE/B3/SUB/2020–243/SI2.826742) programmes.

ORCID

Eliot Durand http://orcid.org/0000-0001-7498-1129
Paul I. Williams http://orcid.org/0000-0002-8973-4718

References

Allied Signals Aerospace. 1996. LF507-1H engine description and operation. Engine manual. Allied Signal Aerospace.

Arnold F, Stilp T, Busen R, Schumann U. 1998. Jetengine exhaust chemiion measurement: Implications for gaseous SO3and H2SO4. Atmos Environ. 32(18):3073–3077.

Burtscher H. 1992. Measurement and characteristics of combustion aerosol with special consideration of photoelectric charging and charging by flame ions. J Aerosol Sci. 23(6): 549–595. https://doi.org/10.1016/0021-8502(92)90026-R

Catalytic Instruments. 2021. Silver particle generator. Instrument manual.

Calcote HF. 1962. Ion production and recombination in flames. In: 8th Symposium (International) on Combustion, Baltimore, MD. p. 184.

CFS Aeroproducts. 2022. ALF502R engine description and operation. Engine manual. CFS Aeroproducts.

Chen X, Jiang J. 2018. Retrieving the ion mobility ratio and aerosol charge fractions for a neutralizer in real-world applications. Aerosol Sci Technol. 52(10):1145–1155. https://doi.org/10.1080/02786826.2018.1498587

Chevron. 2007. Aviation fuels technical review. [accessed 2024 Jul 11]. https://www.chevron.com/-/media/chevron/operations/documents/aviation-tech-review.pdf

Corbin JC et al. 2022. Aircraft particulate matter emissions from conventional and sustainable aviation fuel combustion: comparison of measurement techniques for mass, number, and size. Atmos Meas Tech. 15(10):3223–3242. https://doi.org/10.5194/amt-15-3223-2022

Correa S,M. 1998. Power generation and aeropropulsion of gas turbines: form combustion science to combustion technology. Symp (Int) Combust. 27(2):1793–1807. https://doi.org/10.1016/S0082-0784(98)80021-0

Durand E, Lobo P, Crayford A, Sevcenco Y, Christie S. 2021. Impact of fuel hydrogen content on non-volatile particulate matter emitted from an aircraft auxiliary power unit measured with standardise reference system. Fuel. 287(9):119637. https://doi.org/10.1016/j.fuel.2020.119637

Durdina L et al. 2014. Determination of PM mass emissions from an aircraft turbine engine using particle effective density. Atmos Environ. 99:500–507. https://doi.org/10.1016/j.atmosenv.2014.10.018

Durdina L et al. 2021. Reduction on non-volatile particulate matter emissions of a commercial turbofan engine at the ground level from the use of sustainable aviation fuel blend. Environ Sci Technol. 55(21):14576–14585. https://doi.org/10.1021/acs.est.1c04744

Durdina L et al. 2024. Characterising and predicting nvPM distributions for aviation emissions inventories and environmental impact. Environ Sci Technol. 58(24):10548–10557. https://doi.org/10.1021/acs.est.4c02538

Fialkov A. 1997. Investigation on ions in flames. Progression Energy Combust Sci. 23(5–6):399–528. https://doi.org/10.1016/S0360-1285(97)00016-6

Green JA, Sugden TM. 1963. Some observation on the mechanism of ionisation in flames containing hydrocarbons. Symp (Int) Combust. 9(1):607–621.

Gunn R. 1955. The statistical electrification of aerosol by ionic diffusion. J Colloid Sci. 10(1):107–119. https://doi.org/10.1016/0095-8522(55)90081-7

Haverkamp H, Wilhelm S, Sorokin A, Arnold A. 2004. Positive and negative ion measurements in jet aircraft exhaust: concentrations, sizes, and implication for aerosol formation. Atmos Environ. 38(18):2879–2884. https://doi.org/10.1016/j.atmosenv.2004.02.028

Hayhurst AN, Kittelson DB. 1978. The positive and negative ions in oxy-acetylene flames. Combust Flames. 31:37–51. https://doi.org/10.1016/0010-2180(78)90112-8

Hu X et al. 2022. Morphological and nanostructure characteristics of soot particles emitted from a jet-stirred reactor burning aviation fuel. Combust Flame. 236:111760. https://doi.org/10.1016/j.combustflame.2021.111760

ICAO. 2017. Annex 16 – environmental protection volume II – aircraft engine emissions.

Johnson T,J et al. 2020. Measuring the bipolar charge distribution of nanoparticles: review of methodologies and development using the aerodynamic aerosol classifier. J Aerosol Sci. 143:105526. https://doi.org/10.1016/j.jaerosci.2020.105526

Jung H Kittelson, D, B. 2005. Measurement of electrical charge on diesel particles. Aerosol Sci Technol. 39(12):1129–1135. https://doi.org/10.1080/02786820500430357

Kasper G. 1981. Electrostatic dispersion of homopolar charged aerosols. J Colloid Interface Sci. 81(1):32–40. https://doi.org/10.1016/0021-9797(81)90298-8

Keindler A, Aberle S, Arnold F. 2000. Positive ion chemistry on the exhaust plumes of an aircraft jet engine and a burner: investigation with a quadrupole ion trap mass spectrometer. Atmos Environ. 34(28):4787–4793.

Keindler A, Arnold F. 2002. First composition measurements of positive chemmions in aircraft jet engine exhaust: detection of numerous ion species containing organic compounds. Atmos Environ. 36(8):2979–2984.

Kinsey JS, Hays MD, Dong Y, Williams DC, Logan R. 2011. Physical characterisation of the fine particle emissions from commercial aircraft engines during the aircraft particle emissions experiment (APEX) 1 to 3. Environ Sci Technol. 45(8):3415–3421. https://doi.org/10.1021/es103880d

Kittelson D, B, Pui D, Y, H, Moon, K, C. 1986. Electrostatic collection of diesel particles. SAE Trans. 95(1):51–62.

Kittelson DB et al. 2021. Experimental verification of principal losses in a regulatory particulate matter emissions sampling system for aircraft turbine engines. Aerosol Sci Technol. 56(1):63–74. https://doi.org/10.1080/02786826.2021.1971152

Leppa J, Mui W, Grantz AM, Flagan RC. 2017. Charge distribution uncertainty in differential mobility analysis of aerosols. Aerosol Sci Technol. 51(10):1168–1189. https://doi.org/10.1080/02786826.2017.1341039

Latarche M. 2021. Pounder's marine diesel engines and gas turbines. 10th ed. Butterworth-Heinemann.

Lee, T, W. (2013). Aerospace propulsion. 1st ed. Wiley.

Lidstone-Lane F, O, N, Durand E, F, Williams P, I, Johnson M, Lea-Langton A. 2025. Experimental characterization of electrostatic loss relevant to aviation nvPM sampling. Aerosol Sci Technol. 59(1):79–95. https://doi.org/10.1080/02786826.2024.2390100

Lobo P, Hagen D, E, Whitefield P, D, Raper D.2015. PM emissions measurements of in-service commercial aircraft engines during the Delta-Atlanta Hartsfield study. Atmos Environ. 104:237–245. https://doi.org/10.1016/j.atmosenv.2015.01.020

Lukachko SP, Waitz IA, Miake-Lye RC, Brown RC, Anderson MR. 1998. Production of sulfate aerosol precursors in the turbine and exhaust nozzle of an aircraft engine. J Geophys Res. 103(D13):16159–16174. https://doi.org/10.1029/98JD00684

Malendari C et al. 1975. On the deposition of unipolar charged particles in the human respiratory tract. In: 4th International Symposium of Inhaled Particles and Vapours.

Maricq M, M. 2004. Size and charge of soot particles in rich premixed ethylene flames. Combust Flame. 137(3):340–350. https://doi.org/10.1016/j.combustflame.2004.01.013

Maricq M, M. 2006. On the electrical charge of motor vehicle exhaust particles. J Aerosol Sci. 37(7):858–874. https://doi.org/10.1016/j.jaerosci.2005.08.003

Nishida R et al. 2020. A simple method for measuring fine-to-ultrafine aerosols using bipolar charge equilibrium. ACS Sens. 5(2):447–453. https://doi.org/10.1021/acssensors.9b02143

Nishida R, T, Johnson T, J, Olfert, J, S. 2025. On the three charge regimes of bipolar charge conditioners. Aerosol Sci Technol. 59(5):499–520. https://doi.org/10.1080/02786826.2025.2461161

Olfert J et al. 2017. Effective density and volatility of particles sampled form a helicopter gas turbine engine. Aerosol Sci Technol. 51(6):704–714. https://doi.org/10.1080/02786826.2017.1292346

Ponsonby J, King L, Murray B, J, Stettler M, E, J. 2024. Jet aircraft lubrication oil droplets as contrail ice-forming particles. Atmos Chem Phys. 24(3):2045–2058. https://doi.org/10.5194/acp-24-2045-2024

Savel'ev A, M, Starik A, M, Titova N, S, Favorskii, O, N. 2004. Mechanism of the electrical charging of soot particles upon the combustion of hydrocarbons fuels. Dokl Phys. 49(8):441–446. https://doi.org/10.1134/1.1795954

Savel'ev A, M, Starik A, M. 2001. Dynamics of sulphate aerosol formation in engine jets. Fluid Dyn. 36:95–101.

Sgro L, D'Anna A, Minutolo A. 2010. Charge distribution of incipient flame-generated particles. Aerosol Sci

Technol. 44(8):651–662. https://doi.org/10.1080/02786826.2010.483701

Smith L et al. 2022. Examining chemical composition of gas turbine-emitted organic aerosol using positive matric factorisation (PMF). J Aerosol Sci. 159:105869. https://doi.org/10.1016/j.jaerosci.2021.105869

Sorokin A, Arnold F. 2004. Electrically charged small soot particles in the exhaust of an aircraft gas-turbine engine combustor: comparison of model and experiment. Atmos Environ. 38(17):2611–2618. https://doi.org/10.1016/j.atmosenv.2004.02.032

Sorokin A, Vancassel X, Mirabel P. 2003. Emissions of ions and charged particles by aircraft engines. Atmos Chem Phys. 3(2):325–334. https://doi.org/10.5194/acp-3-325-2003

Starik A, M. 2008. Gaseous and particulate emissions with jet engine exhaust and atmospheric pollution. Adv Propul Technol High-Speed Aircraft. 15:1–15.

TSI. 2016. Electrostatic classifier model 3082 scanning mobility particle sizer (SMPS) spectrometer. Operation and service manual.

Teoh R et al. 2022. Targeted use of sustainable aviation fuel to maximise climate benefits. Environ Sci Technol. 56(23):17246–17255. https://doi.org/10.1021/acs.est.2c05781

Vatazhin A, B, Starik A, M, Cholshchevnikova, F, K. 2004. Electrical charging of soot particles in aircraft engines exhaust plumes. Fluid Dyn. 39(3):384–392. https://doi.org/10.1023/B:FLUI.0000038557.22945.c6

Virtanen A, Marjamäki M, Ristimäki J, Keskinen J. 2001. Fine particle losses in electrical low-pressure impactor. J Aerosol Sci. 32(3):389–401. https://doi.org/10.1016/S0021-8502(00)00087-2.

Xu Z et al. 2024. Assessing the particulate matter emission reduction characteristics of small turbofan engine fuelled with 100% HEPA sustainable aviation fuel. Sci Total Environ. 945:174128. https://doi.org/10.1016/j.scitotenv.2024.174128

Wiedensohler A et al. 2018. Mobility particle size spectrometers: calibration procedures and measurement uncertainties. Aerosol Sci Technol. 52(2):146–164. https://doi.org/10.1080/02786826.2017.1387229

Wiedensohler A. 1988. An approximation of the bipolar charge distribution for particles in the sub-micron range. J Aerosol Sci. 19(3):387–389. https://doi.org/10.1016/0021-8502(88)90278-9

Yu F, Turco RP. 1997. The role of ions in the formation and evolution of particles in aircraft plumes. Geophys Res Lett. 24(15):1927–1930. https://doi.org/10.1029/97GL01822

Yu F, Turco RP. 1998. Contrail formation and impacts on aerosol properties in aircraft plumes: effects of fuel sulphur content. Geophys Res Lett. 25(3):313–316. https://doi.org/10.1029/97GL03695

Yu F, Turco RP. 1999. Evolution of aircraft-generated volatile particles in the far wake regime: potential contributions to ambient CCN/IN. Geophys Res Lett. 26(12):1703–1706. https://doi.org/10.1029/1999GL900324

Zhu J et al. 2024. Inhaled immunoantimicrobials for the treatment of chronic obstructive pulmonary disease. Sci Adv. 10(6):eabd7904. https://doi.org/10.1126/sciadv.abd7904